Melt–crystal density crossover in a deep magma ocean

Razvan Caracas, Kei Hirose, Ryuichi Nomura, Maxim D Ballmer

Earth and Planetary Science Letters 516 (2019) 202–211

Contents lists available at ScienceDirect

Earth and Planetary Science Letters

www.elsevier.com/locate/epsl

Melt–crystal density crossover in a deep magma ocean

Razvan Caracas [a,b,*], Kei Hirose [c,d], Ryuichi Nomura [c,e], Maxim D. Ballmer [c,f,g]

[a] CNRS, Ecole Normale Supérieure de Lyon, Laboratoire de Géologie de Lyon UMR CNRS 5276, 69364 Lyon, France
[b] Center for Earth Evolution and Dynamics (CEED), University of Oslo, Oslo, Norway
[c] Earth-Life Science Institute, Tokyo Institute of Technology, Meguro, Tokyo 152-8550, Japan
[d] Department of Earth and Planetary Science, Graduate School of Science, The University of Tokyo, Bunkyo, Tokyo 113-0033, Japan
[e] Geodynamics Research Center, Ehime University, Matsuyama, Ehime 790-8577, Japan
[f] Institute of Geophysics, ETH Zurich, 8092 Zurich, Switzerland
[g] Department of Earth Sciences, University College London, London, WC1E 6BT, United Kingdom

ARTICLE INFO

Article history:
Received 18 September 2018
Received in revised form 5 March 2019
Accepted 22 March 2019
Available online 2 May 2019
Editor: B. Buffett

Keywords:
magma ocean
density crossover
pyrolite
bridgmanite
molecular dynamics
early Earth

ABSTRACT

The crystallization of a magma ocean (MO) early in Earth's history shaped the entire evolution of our planet. The buoyancy relations between the forming crystals and the residual melt is the most important but also the most unknown parameter affecting the large-scale structure and evolution of the MO. The accumulation of crystals, near the depth of neutral buoyancy between crystals and the coexisting melt, if happening at mid-depths, can separate convecting regions within the MO. Here we use jointly first-principles molecular-dynamics calculations and diamond-anvil cell experiments to obtain the density relations between the molten bulk silicate Earth and the bridgmanite crystals during the crystallization of the MO. The chemical evolutions of the liquid and the coexisting solid during progressive crystallization were constrained by experiments, and the relevant densities were calculated by molecular dynamics. We find that the first crystal of bridgmanite that is formed in a fully molten mantle is Fe-poor, and becomes neutrally buoyant at 110–120 GPa. Since the cooling of the deep MO is fast, and related convection is vigorous, however, first crystals remain entrained. As crystallization advances, the relative Fe content increases in the melt, and the pressure of neutral buoyancy decreases. At 50% solidification, close to the rheological transition, the pressure of the density crossover moves to ~50 GPa. At this pressure, crystals form an interconnected network and block global convection currents, which in turn leads to the separation of the partly crystallized MO into a surficial MO and a basal MO through melt-solid segregation. Such a shallow segregation of a crystal mush at mid-mantle depth has important implications for the dynamics and timescales of early mantle differentiation. Moreover, the shallow segregation should have promoted the formation of a voluminous basal MO that evolves into a large geochemically enriched reservoir. Accordingly, the seismically observed residues of basal MO crystallization in the present-day mantle may host an unmixed reservoir for the missing budget of highly incompatible elements.

1. Introduction

During their formation and early evolution, rocky planets may go through multiple episodes of large-scale melting. The related magma oceans (MOs) were formed by the decay of short-lived radioactive isotopes, potential energy release during core formation and/or large impacts (Elkins-Tanton, 2012). On Earth, planetary-scale melting should have occurred in the aftermath of the giant impact that formed the protolunar disk, and eventually the Earth–Moon system (Canup and Asphaug, 2001; Cuk and Stewart, 2012; Canup, 2012). Independent of the specific scenario for the Moon-forming giant impact, the Earth's mantle must have been largely or even totally molten (Nakajima and Stevenson, 2015; Lock et al., 2018). The solidification and fractionation in this last major MO set up the initial conditions for solid-state mantle convection and geochemical evolution. While the relation between the MO adiabat and the liquidus curve defines the starting point of crystallization (Stixrude et al., 2009), the density relationships between the forming crystals and the residual melts govern the evolution of the MO. End-member scenarios without density crossover in the pressure range of the MO imply a crystallization front that advances downwards from the top or upwards from the bottom. A scenario where the crossover occurs within the pressure range of the MO

* Corresponding author.
E-mail address: razvan.caracas@ens-lyon.fr (R. Caracas).

https://doi.org/10.1016/j.epsl.2019.03.031

eventually leads to crystal accumulation near the crossover depth; subsequently this may lead to separation of the MO into one surficial and one basal MO. Nevertheless, to date, the depth of the density crossover between melt and crystals in the MO remains ill constrained (Labrosse et al., 2007).

Earlier high-pressure melting experiments showed that bridgmanite ($MgSiO_3$-rich perovskite) is the liquidus (first crystallizing) phase for melts formed by partial melting of a pyrolitic mantle above 34 GPa (Ito et al., 2004; Tateno et al., 2014). Bridgmanite remains the only crystalline phase extracted from the melt for more than 50% of the crystallization sequence (Nomura et al., 2014). The timing of the onset of ferropericlase crystallization is important, because it changes the compositional evolution of the residual MO.

Theoretical studies on densities of silicate melts primarily addressed idealized compositions with limited components (e.g., Stixrude et al., 2009; Vuillemieur et al., 2009; Karki, 2010; Bajgain et al., 2015). To our knowledge, there is only one ab initio study of a multicomponent realistic melt (Bajgain et al., 2015), in which the authors reported the variation of melt density with pressure for a mid-ocean ridge basalt (MORB) composition. Similar MORB (Dufils et al., 2017) or volatile-bearing complex silicate melts (Guillot and Sator, 2012) have been examined in other molecular dynamics simulations, but using atomistic empirical models.

However, with these disparate studies, despite their importance, a comprehensive picture of the crystallization history of the entire MO remains elusive to date. Even the debate on the presence of a basal MO remains open as no experimental or theoretical studies have yet been able to confirm the relevant density crossover. Here, we present an effort to determine the relative buoyancy relation between melts and crystals at high pressures and temperatures, which can be used further as an important constraint for the compositional and dynamical evolution of the MO. For this we combine (i) first-principles molecular dynamics simulations, which can accurately yield densities of melts at high pressures and temperatures but fail to provide the chemical evolution of a melt, with (ii) diamond-anvil cell (DAC) melting experiments, which yield the chemical evolution of the melt during its crystallization but fail on determining its density. Finally, the results are (iii) interpreted in a general framework of the crystallizing MO.

2. Methods

2.1. First principles molecular dynamics calculations

We study both melts and crystals employing ab initio molecular dynamics simulations based on the planar augmented wavefunctions (PAW) flavor. We used the VASP implementation (Kresse and Hafner, 1993) with the Gamma point for sampling the Brillouin zone and generalized-gradient approximation for the exchange correlation in the PBE96 formulation (Perdew et al., 1996). We used a kinetic energy cutoff of 550 eV for the planewave basis set and of 800 eV for the augmentation charges.

Because of the presence of iron, all simulations, at all volumes and temperatures are spin-polarized. This allows for the magnetic spin of the individual Fe atoms to be consistently computed at every single time step. We initiate the local magnetic moments with 1 magneton-Bohr par Fe atom. This is enough to break the symmetry of the magnetic wavefunctions that will converge to their state within a few steps.

We also check the behavior of the melt using a +U correction of 4 eV and J correction of 1 eV for the d electrons in two test runs (Anisimov et al., 1991). As expected we see an increase of the magnetic moment of Fe in the melt, and an enhanced alignment of the local magnetic moments of the 4 Fe atoms. This also suggests that simulations using the +U correction clearly preserve the local magnetic moments up to higher pressures. However, due in part to the dilution of Fe in the melt, the equation of state will not change considerably; the values of pressure are similar with and without U within less than 1 GPa.

We ran isokinetic simulations, where the number of particles, volume, and temperature are kept fixed. All simulations were thermalized for at least 1 ps; the timestep was of 1 fs. While such simulations are not micro-canonical, they are good approximations to this ensemble, while being faster; in a way, they are just an extreme version of the Nose-Hoover thermostat where the oscillation period of the temperature is set to the time step. Their major limitations are in preventing us to obtain the specific heat capacity of the melt, as the kinetic energy does not fluctuate. But the equations of state and diffusion properties are similar to the NVT ensembles within the size of error bars (Hernandez and Caracas, 2016).

First the initial melt composition in the calculations was close to the bulk silicate Earth composition (McDonough and Sun, 1995) (Table 1); it corresponds to having a uniform global MO with 0% crystallization. Then we study two more compositions corresponding to 30% and 50% crystallization. The composition of each melt (Table 1) is obtained from melting experiments and partitioning calculations detailed in the next subsection.

Table 1
Compositions of the pyrolitic melts after 0%, 30%, and 50% crystallization. All oxide values are in wt%.

Fully molten mantle							
Ab initio calculation				Pyrolite	Cosm.	E-chondrite	KLB-1
	Atoms		wt%	MS95	PO03	Javoy10	T86
O	89						
Si	24	SiO_2	44.58	45	45.4	51.77	44.48
Al	3	Al_2O_3	4.73	4.45	4.49	1.85	3.59
Fe	4	FeO	8.88	8.05	8.1	9.28	8.1
Mg	30	MgO	37.38	37.8	36.77	35.32	39.22
Ca	2	CaO	3.47	3.55	3.65	1.46	3.44
Na	1	Na_2O	0.96	0.36	0.35	–	0.3
Total	**153**	**Total**	**100**	**99.24**	**98.79**	**99.68**	**99.15**

After 30% crystallization of bridgmanite							
Ab initio calculation				Batch crystal.		Fractional crystal.	
	Atoms		wt%	Mid-LM[a]	Deep-LM[b]	Mid-LM[a]	Deep-LM[b]
O	86						
Si	21	SiO_2	38.96	39.15	39.21	39.08	39.15
Al	3	Al_2O_3	4.72	5.22	5.1	5.31	5.17
Fe	6	FeO	13.31	12.18	12.05	12.29	12.17
Mg	31	MgO	38.58	38.44	38.84	38.23	38.64
Ca	2	CaO	3.46	3.78	3.65	3.84	3.7
Na	1	Na_2O	0.96	1.23	1.15	1.25	1.18
Total	**150**	**Total**	**100**	**100**	**100**	**100**	**100**

After 50% crystallization of bridgmanite							
Ab initio calculation				Batch crystal.		Fractional crystal.	
	Atoms		wt%	Mid-LM[a]	Deep-LM[b]	Mid-LM[a]	Deep-LM[b]
O	81						
Si	18	SiO_2	34.38	32.13	32.23	31.86	32
Al	3	Al_2O_3	4.86	5.6	5.37	5.93	5.64
Fe	7	FeO	15.99	16.2	15.82	16.7	16.4
Mg	30	MgO	38.44	40.53	41.45	39.66	40.61
Ca	3	CaO	5.35	4.02	3.79	4.23	3.93
Na	1	Na_2O	0.99	1.52	1.33	1.61	1.43
Total	**143**	**Total**	**100**	**100**	**100**	**100**	**100**

Note: MS95 = McDonough and Sun, 1995; PO03 = Palme and O'Neill, 2003; Javoy10 = Javoy et al., 2010; T86 = Takahashi, 1986.

[a] Calculated using partition coefficients obtained at 74 GPa in Nomura et al. (2011) from the fully molten mantle composition employed by the ab initio simulations.

[b] Same as above, but calculated using partition coefficients obtained at 132 GPa (Nomura et al., 2011). LM = lower mantle.

In the *ab initio* simulations, melts were obtained starting from a crystalline silicate with the appropriate chemical compositions. Cations were placed on a lattice based on their nominal valence; we overheated this structure to 5000 K to induce melting and then brought the temperature to the desired value for production runs. The high temperatures we reached during melting and the long thermalization runs (several picoseconds) ensure that the local structure in the resulting melts is at equilibrium, as confirmed by diffusion tests. All the simulation boxes of the melt were cubic, and contained 153, 150, and 143 atoms respectively for the melts after 0%, 30%, and 50% crystallization. The numbers of atoms in our simulations are in the middle range of similar simulations on silicate systems (e.g., Stixrude and Karki, 2005; Ghosh and Karki, 2011; Bajgain et al., 2015; Green et al., 2018); we are also able to fit each oxide component estimated from the experiments to better than 1 wt%.

For each of the three melt compositions we performed calculations along the 3000 K, 4000 K, and 5000 K isotherms. We start at low density, typical ambient density conditions, and we increase the pressure by taking a snapshot from a thermalized melt and uniformly decreasing the volume of the simulations cell. This reproduces a step-by-step pressure increase as obtained in standard high-pressure DAC experiments. In this way we go to pressures beyond 150 GPa, which allow us to better constrain the equations of state up to lower-mantle pressures and temperatures.

The computed density–pressure points for the melts in our simulations are best fitted with 3rd order Birch-Murnagham equations of state (EOS) at each isotherm. For the pyrolite melt prior to crystallization the best single fit to all the computed density–pressure–temperature points is obtained with (i) a 3rd order Murnagham EOS:

$$P_{VT} = \frac{K_{0T}}{K'_{0T}}\left[\left(\frac{V_{0T}}{V}\right)^{K'_{oT}} - 1\right], \tag{1}$$

where P is pressure, K is bulk modulus, K' is its derivative with respect to pressure, and V is volume, and (ii) the thermal expansion according to the modified Holland-Powell (Holland and Powell, 1998) equation:

$$V_{0T} = V_{00}\big(1 + \alpha_0(T - T_0) - 2\alpha_1(\sqrt{T} - \sqrt{T_0})\big), \tag{2}$$

where α_0 and α_1 are thermal expansion coefficients. Subscript zero denotes the reference pressure, i.e. 0 GPa, or temperature, in our case 3000 K.

We have also calculated the densities of $MgSiO_3$ and $Mg_{0.75}Fe_{0.25}SiO_3$ bridgmanite along the 3000 K and 4000 K isotherms to bracket that of realistic Fe-bearing bridgmanite. Higher temperatures might melt the crystals or at least bring them in an unstable overheated state. We also allow the Fe atoms in bridgmanite to be magnetic, with similar settings as for the pyrolite melt; they preserve their magnetization up to at least 125 GPa at 4000 K. At high temperatures and pressures the density of our computed solid $MgSiO_3$ bridgmanite agrees within 2.3% or better with previous values published in the literature (Stixrude and Karki, 2005). We interpolated the density of the crystals with intermediate Fe contents using a linear approximation between these two compositions.

2.2. High-pressure melting experiments

New melting experiments were carried out at 59 GPa and 115 GPa in a laser-heated DAC to examine the liquidus phase during the latter stage of solidification of a magma ocean and to improve the determination of the Fe partitioning coefficients between the melts and the bridgmanite crystals, as well as to refine the chemical evolution of the magma ocean during its crystallization. We prepared starting materials with compositions formed by 50% fractional crystallization of bridgmanite from a pyrolitic melt under middle and deep lower mantle conditions (see the Results section for details). These starting compositions were calculated with partition coefficients obtained by Nomura et al. (2014) at 74 and 132 GPa, respectively (Table 1). A difference in the mode of crystallization (batch or fractional) results in a minor difference in the major element composition of residual melts.

Samples were synthesized from gel and dehydrated at 1273 K for 30 min in a CO_2–H_2 gas flux furnace, in which oxygen fugacity was held above the iron-wüstite buffer. Compositional homogeneity was confirmed by electron microprobe analyses. The samples were pressed to a disk and loaded into a hole with a diameter of 35 or 100 µm in a rhenium gasket preindented to a thickness of 40 or 60 µm, respectively. We used no thermal insulator in order to avoid chemical reactions. After sample loading, the whole DAC was dried in a vacuum oven at 393 K for at least 12 hr before compression. The sample was heated from both sides by an Yb fiber laser (*SPI*) with a focused beam size of 30 µm. We applied a target laser output power from start and heated the sample for 5 s. Pressure was measured via the Raman shift of diamond at room temperature after heating and corrected for thermal pressure following Nomura et al. (2014).

The melting of a sample was easily recognized by its texture from a stereoscopic observation; the center of a heating spot became opaque with a spherical shape upon melting. After complete pressure release, the sample was recovered from the DAC and glued onto a silicon wafer using G2 epoxy resin. It was polished by Ar ions in an Ion Slicer (*JEOL* EM-9100 IS) parallel to the compression axis. The final thickness of the polished sample was controlled to be 10 µm, which is thick enough to be regarded as infinite for microprobe analysis (Wade and Wood, 2012). Textural observations and chemical analyses were made by a field emission-type electron probe micro-analyzer (FE-EPMA: *JEOL* JXA-8500F/8530F) with an accelerating voltage of 10 kV and a current of 12 nA (Figs. 1 and S1). The x-ray counting time for peak/background was 20/10 s for Si, Ca, Fe, Al, and Mg, 10/5 s for Na, and 8/4 s for K. Both Na and K were analyzed first to minimize volatile loss. Wollastonite (for Si, Ca), K-feldspar (for K), albite (for Na), corundum (for Al), periclase (for Mg), and hematite (for Fe in silicate) were used for standards in FE-EPMA analyses. PETJ (Ca, K), TAP (Si, Al), TAPH (Na, Mg), and LIFH (Fe) were applied as analyzing crystals.

3. Results

3.1. Compositional evolution of a magma ocean

Concerning the first stage of the crystallization, *i.e.* the extraction of bridgmanite, based on our previous experimental data (Nomura et al., 2014), we obtained the partition coefficients between melt and bridgmanite at 74 and 132 GPa. The partition coefficient D_x of oxide x is defined as the ratio between the weight concentrations in crystal and melt:

$$D_x = \frac{C_x^{crystal}}{C_x^{melt}} \tag{3}$$

The results show the D_x is 0.69(5) for Al_2O_3, 0.10(2) for FeO, 0.73(11) for CaO, and 0.27(5) for Na_2O (the same value was assumed for K_2O) at 74 GPa, and 0.76(11) for Al_2O_3, 0.12(5) for FeO, 0.83(17) for CaO, and 0.44(12) for Na_2O at 132 GPa.

Then using these bridgmanite/melt partition coefficients obtained at 74 and 132 GPa, we calculate the compositional evolutions of both bridgmanite and melts with progressive magma

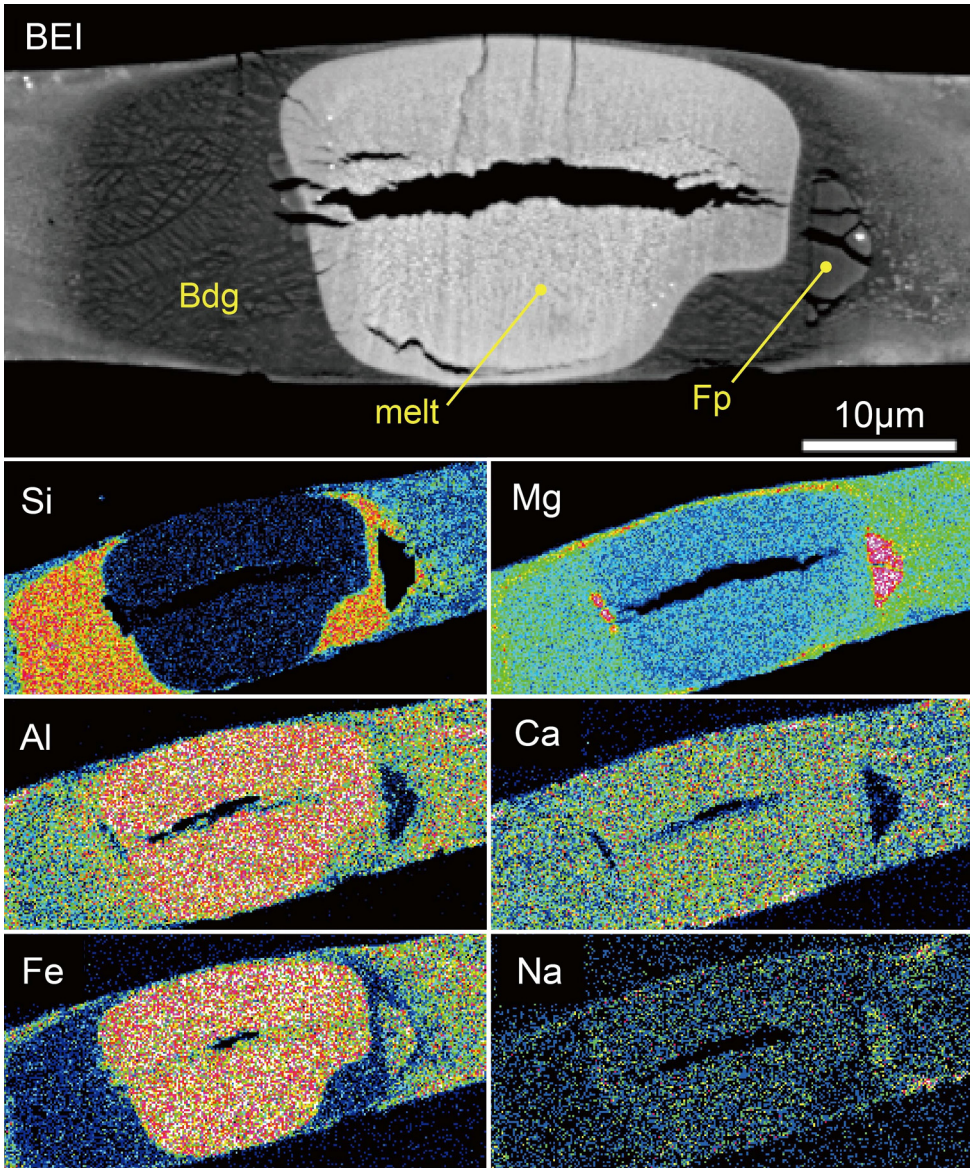

Fig. 1. Melting experiment on the evolved magma composition formed after 50% solidification from a fully molten mantle (Table 1). Backscattered electron image (top) and the X-ray maps for Si, Mg, Al, Ca, Fe, and Na obtained in run #1 at 59 GPa. The Fe-rich melt crystallizes $MgSiO_3$-rich bridgmanite and a trace amount of (Mg,Fe)O ferropericlase at total 67% solidification from a fully molten pyrolite.

ocean solidification under mid-lower mantle and deep lower mantle conditions, respectively. The Al_2O_3, FeO, CaO, and Na_2O contents in bridgmanite ($C_x^{crystal}$) were determined as:

$$C_x^{crystal} = C_{x0}^{melt} x D_x x F^{(D_x - 1)} \quad \text{(fractional crystallization)} \tag{4}$$

$$C_x^{crystal} = \frac{C_{x0}^{melt} x D_x}{F(1 - D_x) + D_x} \quad \text{(batch crystallization)} \tag{5}$$

where F and C_{x0}^{melt} are the weight fraction of melt and the initial concentration of oxide x in the melt, respectively. The MgO and SiO_2 contents in bridgmanite were obtained from its stoichiometry. We then calculated a residual melt composition from that of bridgmanite. The chemical compositions of the evolved magma ocean (after 30% and 50% crystallization from a fully molten mantle with a composition close to pyrolite) are given in detail in Table 1. These calculated compositions are extremely similar to the ones directly measured on the residual melts in our diamond-anvil experiments (Table 2).

Our partitioning calculations indicate that, with advancing crystallization of bridgmanite, the melt becomes depleted in the MgO and SiO_2 components, and enriched in CaO, Al_2O_3, and most importantly FeO compared to the initial pyrolite composition. After 30% batch crystallization in the mid-lower mantle (Table 1), the FeO content is enhanced from 8.9 to 12.2 wt%, while SiO_2 is depleted from 44.6 to 39.2 wt%. Between 30% and 50% crystallization, the relative FeO content increases by another 4.0 wt%, and SiO_2 is depleted by another 7.0 wt%. The evolution of the composition of major elements is only weakly affected by the mode of crystallization: the difference between batch and fractional crystallization is as small as the variation between the model compositions for a 'primitive mantle'.

The experiment on pyrolite at 74 GPa (Nomura et al., 2014) included 55 wt% melt, 43 wt% bridgmanite, and negligible amounts of ferropericlase (1 wt%) and $CaSiO_3$ perovskite (1 wt%). To address the late crystallization stage, in this study, we performed a series of new melting experiments on residual melt compositions formed after 50% solidification (Table 1). At 59 GPa (run #1), the sample included 33 wt% crystals and 67 wt% quenched melt, corresponding to total 67% ($= 50 + 50 \times 0.33\%$) crystallization from a pyrolitic melt (Table 1). The sample cross-section shows that the melt

Table 2
Chemical compositions of the quenched silicate melts and liquidus phases (wt%).

Run#	1	2
Pressure (GPa)[a]	59	115
Starting material		
SiO_2	34.85	35.09
Al_2O_3	5.71	5.42
FeO	15.42	15.16
MgO	39.03	39.71
CaO	4.51	4.19
Na_2O	0.44	0.39
K_2O	0.04	0.04
Quenched silicate melt		
SiO_2	28.28(54)	32.87(18)
Al_2O_3	8.00(24)	7.25(8)
FeO	18.01(40)	12.28(38)
MgO	31.98(60)	35.81(45)
CaO	4.11(25)	3.99(7)
Na_2O	0.20(3)	0.10(2)
K_2O	0.34(6)	0.24(9)
Total	**90.91(105)**	**92.53(69)**
Bridgmanite		
SiO_2	56.92(91)	55.43(106)
Al_2O_3	4.84(36)	4.92(50)
FeO	2.03(32)	1.34(7)
MgO	34.23(73)	35.31(54)
CaO	3.63(37)	2.83(47)
Na_2O	0.04(1)	0.04(2)
K_2O	<DL[b]	<DL[b]
Total	**101.70(70)**	**98.91(70)**
Ferropericlase		
SiO_2	0.44(13)	
Al_2O_3	1.62(11)	
FeO	10.31(37)	
MgO	82.89(24)	
CaO	0.13(3)	
Na_2O	0.43(5)	
K_2O	<DL[b]	
Total	**95.83(37)**	

[a] Pressure was determined from the Raman peak shift of diamond at 300 K after experiments.
[b] <DL, below detection limit of the microprobe analyses.

coexisted with both bridgmanite and ferropericlase (Fig. 1), but the latter is a minor phase. In the 115 GPa sample (run #2), a crystal fraction was calculated to be 55 wt%, indicating total 77% (= 50 + 50 × 0.55%) crystallization from a fully molten pyrolite (Table 1). The melt has been in contact with bridgmanite only (Fig. 1), which is consistent with its larger liquidus field with respect to that of ferropericlase at higher pressures. These results indicate that the crystallization of ferropericlase is negligible in a magma ocean at pressures greater than 59 GPa until >60% solidification.

3.2. Densities of melt and crystals at high P-T

On the basis of these experimental findings for MO solidification and crystal compositions, we use the experimental compositions of the residual melts to calculate the melt densities. We examine a fully molten pyrolitic mantle, and residual melts after 30% and 50% crystallization along three isotherms, 3000 K, 4000 K, and 5000 K, to pressures beyond 150 GPa from first-principles molecular dynamics. We also compute the density of bridgmanite crystals using consistently the same methods and parameters at 3000 and 4000 K. These calculations cover the entire thermochemical space of MO solidification up to 50% crystallization. A degree of crystallization of ∼50% is thought to mark the rheological transition, at which crystals form an interconnected network (Abe, 1995; Costa et al., 2009). Before the rheological transition (low crystallinity), melts behave similar to liquids with very low viscosities. After the transition (high crystallinity), the partial melt (or crystal mush) behaves more similarly to a solid with a viscosity that is several orders of magnitude higher than that of the liquid.

Table 3
Computed pressure (in GPa) along the three isotherms for the three chemically distinct melt compositions, in the melt simulations for various densities.

Density (g/cm^3)	$T = 3000$ K	$T = 4000$ K	$T = 5000$ K
0% crystals			
5.377	138.6(10.9)	147.3(3.2)	157.9(3.2)
4.645	73.1(9.4)	83.8(2.7)	91.7(3.3)
4.040	41.4(2.6)	48.0(2.8)	53.6(2.8)
3.535	22.7(1.7)	27.0(2.4)	31.2(2.4)
3.111	11.8(1.6)	14.5(1.9)	17.5(2.0)
2.753	4.8(1.4)	7.1(1.7)	9.3(1.9)
2.447	1.3(1.3)	2.9(1.5)	4.6(1.6)
2.185	−0.6(1.3)	0.6(1.4)	
1.947		−0.2(1.3)	0.5(1.2)
30% crystals			
6.278			255.1(3.8)
5.719	169.0(1.9)		
5.383	132.1(2.1)	138.9(2.5)	149.1(3.1)
4.650	70.3(2.1)	78.1(4.1)	87.0(2.9)
4.044	38.4(2.3)	45.0(2.9)	50.7(2.6)
3.539	21.1(1.8)		
3.115	10.7(1.6)	13.0(1.8)	16.4(2.0)
2.738	4.4(1.5)	6.2(1.7)	6.8(1.6)
2.434	1.1(1.5)	2.5(1.3)	4.1(2.0)
2.174	−0.7(1.1)	0.5(1.3)	
1.949			−0.3(1.3)
50% crystals			
6.290	203.4(2.4)	212.8(2.9)	223.9(3.3)
5.393	111.9(2.2)	120.6(2.7)	129.7(3.0)
4.658	60.4(2.1)	68.0(2.6)	75.8(3.1)
4.052	32.9(2.7)	38.4(2.4)	43.8(2.5)
3.121	8.0(1.4)	10.6(2.1)	13.9(2.0)
2.455	0.2(1.3)	1.6(1.5)	3.3(1.9)
2.124	−1.0(1.3)	0.0(1.2)	2.7(1.5)
1.904		−0.5(1.1)	0.3(1.2)

The densities of the pyrolite melt for the three degrees of crystallization (0%, 30%, 50%) and for the three temperatures (3000, 4000, 5000 K) considered here are given in Table 3. To validate our calculations into perspective, we calculate the density of the theoretical pyrolite melt at 2650 K and 25 GPa. We find that our results are similar (i.e. <4% difference, on the order of the size of our data points) than those from flotation experiments at the same thermodynamical conditions (Suzuki and Ohtani, 2003).

The calculated densities of the melts are fitted separately along each isotherm with a 3rd order Birch-Murnagham EOS (Tables S1 and S2). The thermal expansion varies with pressure, being less important at greater depths, where the slope of the compressibility flattens out. The temperature response is almost linear with a reduction of about 0.1 g/cm^3 for each increase in temperature of 1000 K, under core–mantle boundary pressure. The 30% crystallization leads to a melt density increase of 0.05–0.1 g/cm^3; this increase is systematically larger at higher pressures and temperatures. Advancing crystallization from 30% to 50% has even larger implications in terms of melt densities; there is an additional increase of about 0.15–0.2 g/cm^3, which again tends to be stronger for higher pressures and temperatures. At the same time, the density of bridgmanite that is in equilibrium with the progressively FeO-enriched liquid increases by about 0.2 g/cm^3 upon replacement of 25% Mg by Fe in the crystal structure.

3.3. Other physical properties of the pyrolite melts

The densification of the melts at high pressure is accommodated by increasing the coordination numbers of cations by oxy-

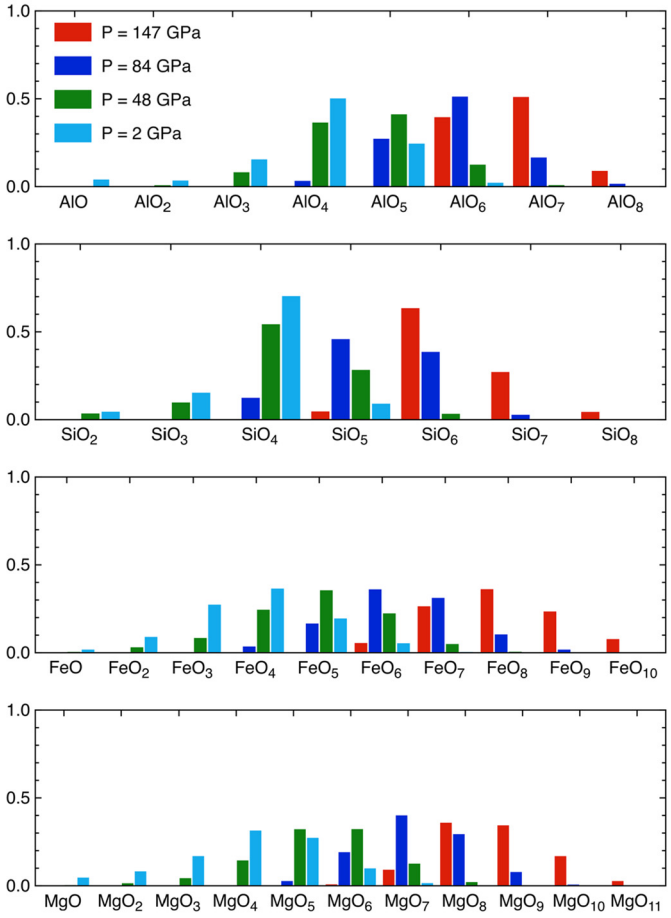

Fig. 2. Speciation in the pyrolite melt at several pressures along the 4000 K isotherm. Pressure is accommodated by the increasing number of coordination, clearly seen in all cation-oxygen pairs. Vertical scale gives the relative ratio of each species, with 1.0 being the total amount of species. Color indicates pressure, as shown in the legend. (For interpretation of the colors in the figure(s), the reader is referred to the web version of this article.)

gen. At low pressures, SiO_4 and AlO_4 tetrahedra dominate the speciation of the melts (Figs. 2 and S2). The tetrahedra are mostly isolated and have individual lifetimes on the order of a picosecond or more. Since the other cations are highly diffusive they do not form clear long-lasting coordination polyhedra. As pressure increases, the speciation is dominated by polyhedra with progressively higher coordination numbers: Si forms SiO_5 pentahedra, and eventually SiO_6 octahedra and SiO_7 groups, Al forms AlO_5, then AlO_6 and AlO_7. At the bottom of the magma ocean most of Fe is surrounded by 7 or 8 O atoms, and Mg by 8 or 9 (Fig. 2). The silica and alumina polyhedra start to polymerize to compensate for the increased coordination. In this pressure range, *i.e.* ambient to bottom of the magma ocean, the interatomic distances decrease by not more than 10% (Fig. S2). These observations are consistent with other molecular dynamics studies of silicate melts (e.g., Stixrude and Karki, 2005; Ghosh and Karki, 2011; Bajgain et al., 2015).

The melts have metallic magnetic character; the individual spins on the Fe atoms are non-zero at low pressures, oscillating between up and down states, with a local magnetic moment usually close to 4 magneton-Bohrs (Fig. S3). With increasing compression, the oscillating character intensifies, and the individual magnetic moments pass more and more time in intermediate values close to 2. As a result, at 4000 K and 85 GPa, iron is up to 25% of the time in intermediate spin configuration close to 2. But even at the pressures and temperatures characteristic to the bottom of the magma ocean the individual magnetic moment on the iron atoms is still non-null; the full spin transition occurs at pressures beyond 150 GPa (Fig. S3).

Finally, the self-diffusion coefficients for the elemental species in the melt (Fig. 3) obtained as the linear slope of the corresponding mean square displacement versus time (Fig. S4), decrease quasi-linearly with pressure in a log plot. The most diffusive elements are Mg and Fe, with Si and Al being the least diffusive. The three distinct chemical compositions of the pyrolite melt show similar diffusion coefficients, suggesting that the major factors that affect the transport properties of the melt, including viscosity, are the temperature and the pressure of the MO, or perhaps the presence of volatiles (Dingwell, 2006), but not FeO content. Accordingly, the viscosity of the melt will not evolve considerably during crystallization, at least up to 50% solidification. It is the formation and configuration of solid crystals, as well as the accumulation of crystals according to the buoyancy relations, that will affect the bulk transport properties of the mush, and actual flow of matter across the MO.

4. Discussion

4.1. Density crossover between crystals and residual melts in the MO

We compare the computed densities of the melt with those of the coexisting bridgmanite crystals at three stages of solidification (Fig. 4). We define the density crossover depth (DCD) as the depth at which the densities of the two phases are equal and the system reaches neutral buoyancy. The DCD as a function of crystallinity is the result of the interplay between temperature, iron content in crystallizing bridgmanite, and the melt chemical evolution. The first crystal that formed from a fully molten pyrolite is neutrally buoyant in the lowermost part of the MO, just above the core–mantle boundary, at pressures of about 110–120 GPa at a liquidus temperature of 4000–5000 K (Fiquet et al., 2010; Andrault et al., 2011) (Fig. 4A). After 30% crystallization, the removal of Si and the relative enrichment in Fe densify the residual melt. In this context the pressure of the neutral buoyancy region rises to about 80 GPa (Fig. 4B). At 3000–3500 K, at 50% crystallization (Fiquet et al., 2010; Andrault et al., 2011), by the time the bridgmanite crystals form an interconnected network at the rheological transition (Abe, 1995; Costa et al., 2009), neutral buoyancy occurs at around 50 GPa (DCD $\approx$ 1250 km) (Fig. 4C).

The present experiments demonstrate that the bridgmanite/melt partition coefficient, D_{FeO}, is about 0.1 in an evolved pyrolite system (Tables 1 and 2), consistent with previous measurements under deep lower mantle conditions (Nomura et al., 2014; Ito et al., 2004). Recent melting experiments on MORB (Pradhan et al., 2015) also reported similar Fe/Mg distribution coefficient K_D. On the other hand, Andrault et al. (2012) demonstrated remarkably higher D_{FeO} values, $\sim$0.55 at 50 GPa and $\sim$0.5 at 135 GPa. If we employ $D_{FeO} = 0.55$, a residual melt after 50% batch (fractional) crystallization contains 11.5 (12.3) wt% FeO, which coexists with bridgmanite with Fe/(Mg+Fe) molar ratio of 0.103 (0.112). Accordingly, the density crossover between the melt after 50% solidification would be shifted to 65 GPa for $D_{FeO} = 0.55$ (Fig. 4C), which is however not much different from the 50 GPa obtained with $D_{FeO} = 0.1$. The dependence of DCD on Fe partitioning is shown in Fig. 4 by the width of the neutral buoyancy regions.

4.2. Formation of a basal magma ocean

The melt–crystal DCD has profound dynamical implications on the cooling and geochemical evolution of the MO. Depending on the mode of crystallization (fractional vs. batch) and the depth of the onset of crystallization, we can separate four end-member

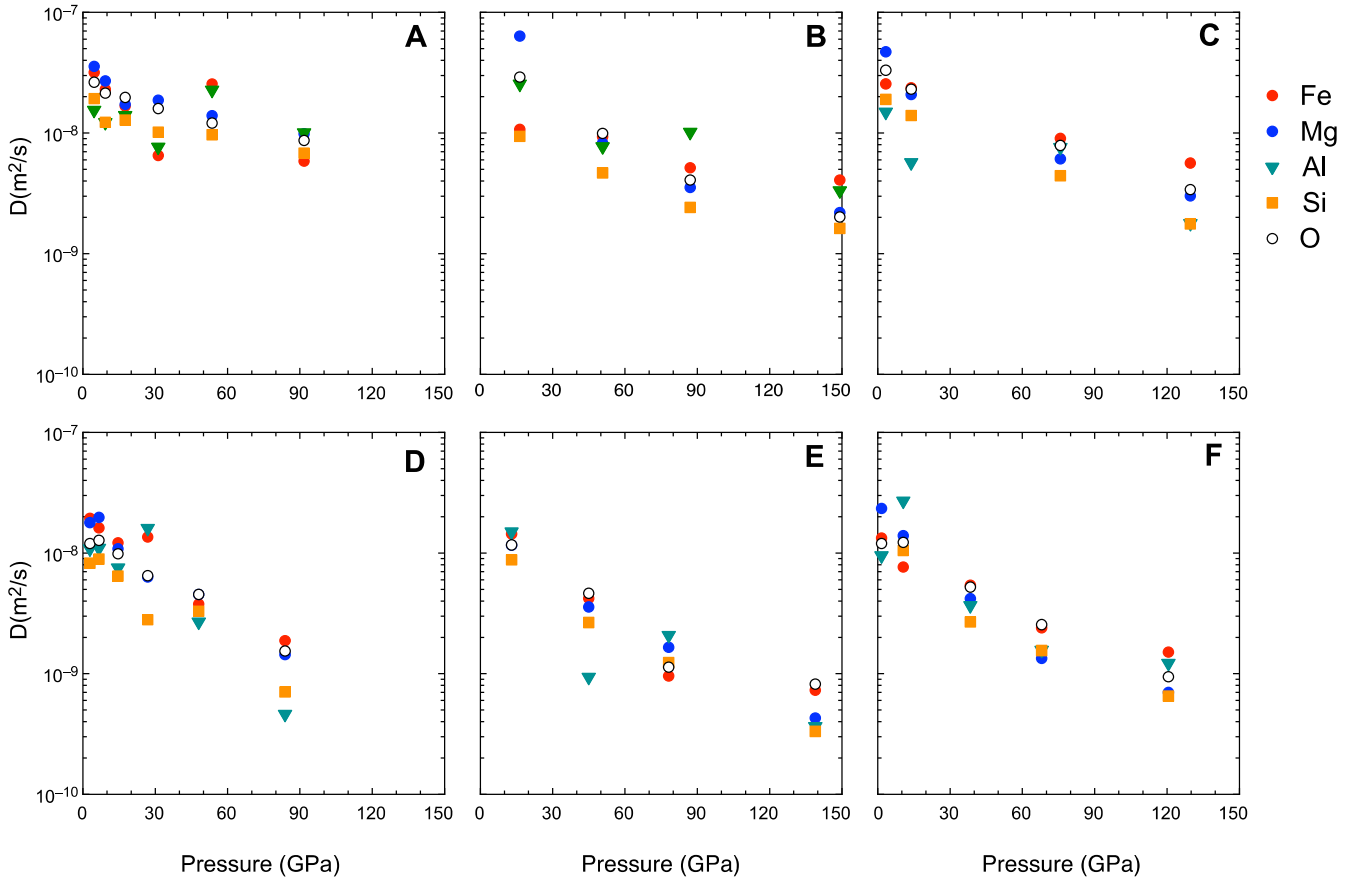

Fig. 3. Self-diffusion coefficients for selected elements in melts. Coefficients are computed at 5000 K (A, B, C) and 4000 K (D, E, F) in a pyrolitic melt prior to crystallization (A, D), and in evolved melts after 30% (B, E) and 50% crystallization (C, F).

scenarios (Fig. 5). The onset of crystallization occurs at the intersection of the adiabat and the liquidus. Fractional crystallization is dominant for a relatively slowly convecting MO, that can be achieved for example due to the presence of a thermally insulating atmosphere, which reduces the heat flux out of the MO (Elkins-Tanton, 2012; Hamano et al., 2013; Lebrun et al., 2013). For relatively slow cooling of the MO, Stokes sinking velocities of crystals are faster than characteristic convective velocities (Tonks and Melosh, 1990). On the other hand, batch crystallization is dominant for vigorous convection in the liquid due to fast MO cooling with efficient radiation of heat into space, such that crystals remain entrained (Solomatov, 2015).

4.2.1. The fractional crystallization case

For the fractional crystallization end-member (i.e. at infinitely small crystallinity), crystals rise as long as crystallization starts below the DCD (corresponding to ∼115 GPa). They will melt during their ascent as they intersect the liquidus (i.e., decompression melting; Fig. 5A), pumping SiO_2 upward and leaving a stably stratified zone at the base of the MO that is enriched in FeO. As the MO cools, and this decompression melting becomes more and more limited, and crystals will ultimately be stabilized at ∼115 GPa to separate the BMO from the shallow MO. In this case, the initial BMO will be moderately enriched in FeO relative to pyrolite. If the onset of the crystallization takes place at the DCD, no rising or remelting occurs, and the initial composition of the BMO will not be enriched in FeO. If crystallization starts above the DCD (Fig. 5B), crystals will sink and remelt (as in this case the adiabat would be less steep than the liquidus), pumping SiO_2 downward. However, this unstable stratification will immediately be erased by MO convection in the liquid MO, and crystallization will continue without making stratification until the crystallizing Fe-poor crystals accumulate at the DCD and separate the BMO with a pyrolitic initial composition. Thus, for fractional crystallization, the initial BMO is predicted to be relatively small with a depth extending from the core–mantle boundary to ∼2500 km, and moderately FeO-enriched (i.e., if the onset of crystallization is deeper than the DCD; Fig. 5A) to pyrolitic in composition (Fig. 5B).

4.2.2. The batch crystallization case

In the case of batch crystallization, crystals remain in thermal and chemical equilibrium with the coexisting MO. The partially crystallized MO convects with a similar vigor as the overlying fully molten MO, and crystals remain entrained. In contrast to the former scenario, vigorous MO convection can preclude any crystal settling and fractional crystallization (Solomatov, 2015). Entrainment of crystals in a vigorously convecting MO (with continuous remelting and partial crystallization during convective cycles) continues until the rheological transition is reached at ∼50% crystallization.

At the rheological transition, the melt-crystal mixture (mush) becomes significantly more viscous (Abe, 1995; Costa et al., 2009), as crystals start to form an interconnected network. Accordingly, MO convection ceases, and compositional fractionation of the mush into a cumulate and coexisting melt ultimately occurs due to compaction.

According to our density calculations, this compaction is accommodated by downward melt migration below the DCD, and upward melt migration above the DCD. Thus, a basal MO emerges out of a thick downward-compacting mush layer that reaches from ∼1250 km depth (50 GPa) to the CMB (Fig. 5C). As the mush layer compacts, it segregates into a dense FeO-rich melt that percolates downward and a Fe-poor crystalline cumulate layer that

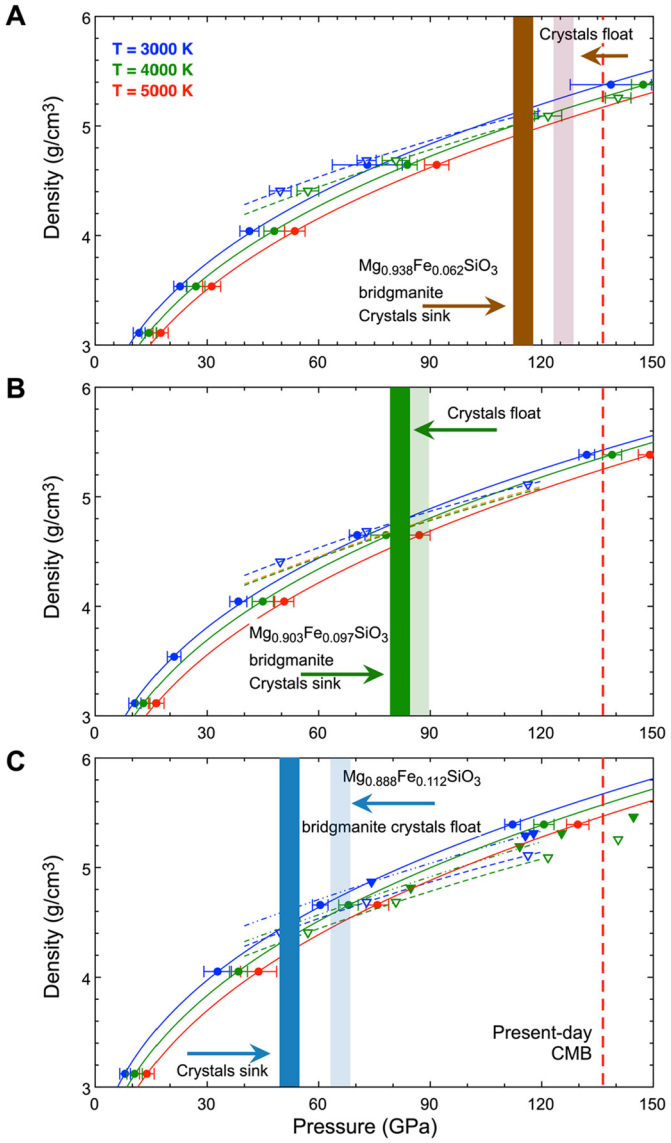

Fig. 4. Densities for melts and bridgmanite crystals. Densities are calculated at temperatures of 3000 K, 4000 K, and 5000 K (colors) for tow sets of bridgmanite crystals ($MgSiO_3$, open triangles, dashed lines; $Mg_{0.75}Fe_{0.25}SiO_3$, closed triangles, dashed-dotted lines) and after 0% (A), 30% (B), and 50% (C) crystallization for melts (circles, solid lines). We linearly interpolate the densities of the solids as a function of Fe. Considering our partitioning coefficients, the Fe contents of the solids would vary with crystallization as indicated in the three panels. With these estimates, the density crossover between melt and crystals occurs at ~115 GPa, ~80 GPa, and ~50 GPa at 0%, 30%, and 50% solidification (colored opaque vertical bars), respectively. The relevant temperatures are 3000–4000 K (at ~50 GPa) and 4000–5000 K (~115 GPa). As stronger Fe partitioning into bridgmanite is considered (Andrault et al., 2012), the crossover is shifted to slightly higher pressures (translucent bars). The presence of Al would render perovskite denser than the pure end-member term, but lighter than the Fe-bearing ones.

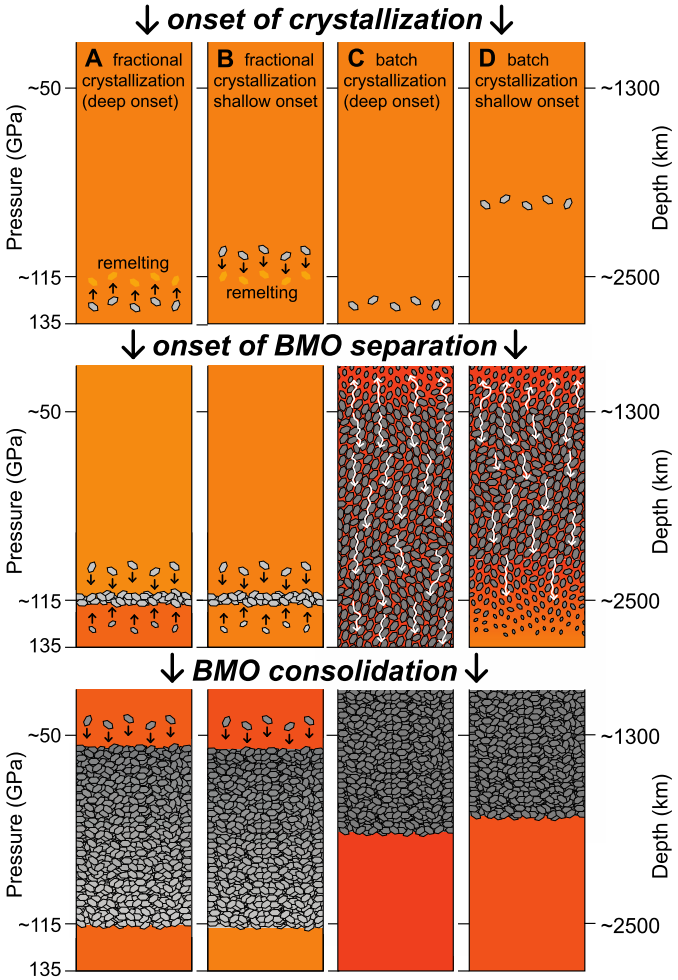

Fig. 5. Solidification of a deep magma ocean. Four different scenarios are considered, depending on the mode of crystallization and the depth at which solidification starts; fractional (A, B) or batch crystallization (C, D), and deep (A, C) or shallow onset of crystallization (B, D). The color reflects the degree of enrichment in incompatible elements including iron.

floats above. The initial composition of the BMO is that of the liquid in the mush (Table 1, bottom), or slightly less enriched in FeO if the onset of crystallization occurs close to the DCD at ~1250 km depth (50 GPa) (Fig. 5D).

While none of the above scenarios can be excluded (Solomatov, 2015), we favor batch crystallization in the lower mantle over fractional crystallization. Previous work consistently showed that the early hot days of a deep MO with very high surface temperatures are associated with very fast cooling, and thus vigorous MO convection (Solomatov et al., 1993; Lebrun et al., 2013; Bower et al., 2018). In Fig. 6, we show MO surface heat flux as a function of MO depth extent for various MO cooling scenarios and mantle liquidi. Comparison with the expected transitional heat flux for crystal settling elucidates that batch crystallization is favored for all cooling scenarios and mantle liquidi considered.

4.2.3. The initial volume and composition of the basal magma ocean

Between the two batch-crystallization scenarios (Fig. 5C, 5D), we further favor the scenario with a pervasive mush in the lower mantle just before the onset of compaction (Fig. 5C). Considering that partial-melt adiabats are generally sub-parallel to the melting curve (see e.g. Fig. 3 in Bower et al., 2018), the crystallinity of the mush should be at or very near the rheological transition everywhere below the DCD, independent of the exact depth of onset of crystallization. This sub-parallelism is related to the consumption/release of latent heat during (adiabatic) heating/cooling of the mush in a partial melt. Adopting this scenario (Fig. 5C) as the most likely scenario, we can further constrain the initial composition and volume of the BMO.

For example, the sub-parallelism between the partial-melt adiabat and the melting curve allows to exclude downward freezing during melt percolation as a dominant process. Also, as the mush thermal profile is near adiabatic, mush-state convection should be a rather inefficient process of material transport, and downward percolation should indeed dominate. In any case, regardless of the mechanism of material transport, only minor partial refreezing

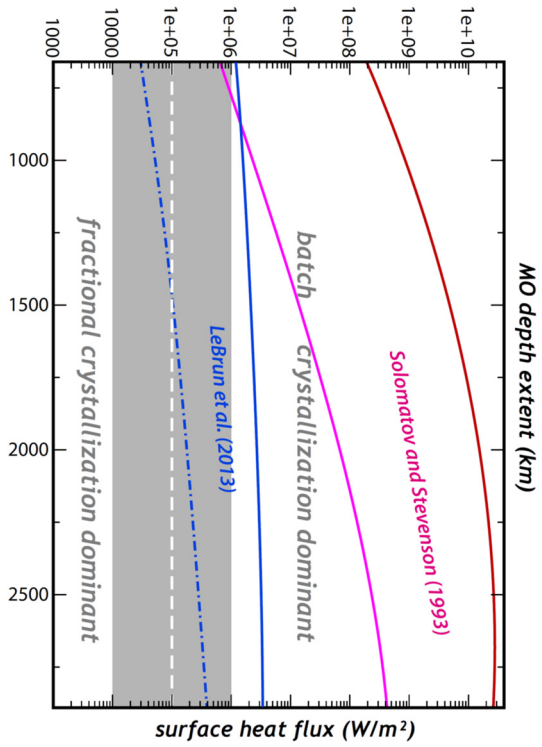

Fig. 6. Estimation of crystallization mode in a deep magma ocean. Heat flux out of the MO according to MO cooling parameterizations as a function of MO depth extent (colored lines). Warm-colored lines provide upper bound scaling by Solomatov et al. (1993), based on a simple black-body radiation, and no shielding atmosphere is present. Liquidi in pink (Andrault et al., 2011) and red (Fiquet et al., 2010) are used to scale from surface temperature to MO depth. Blue lines provide lower bound scaling by Lebrun et al. (2013) with a steam atmosphere that is progressively exhaled from the MO (dashed-dotted) and no atmosphere (solid). According to Solomatov (2015), the transitional heat flux between fractional and batch crystallization is $\sim 10^5$ W/m^2 (dashed white line), albeit with significant error bars (gray bar). In the relevant depth range for BMO formation, estimates for MO surface heat flux are systematically higher than 10^5 W/m^2.

during downward segregation is expected to occur, and thus only minor fractionation that could otherwise reduce the initial volume and increase the initial FeO content of the BMO is expected. Under the assumption of parallelism between partial-melt adiabats and the melting curve, the initial composition of the BMO is fully constrained by our melting experiments at 50% crystallization (Table 1, bottom), and the initial volume is ~50% of that of the mush layer of thickness ~1640 km. Accordingly, the initial BMO extends from the core–mantle boundary to ~2000 km depth (Fig. 5C). Even if the assumption of parallelism is somewhat relaxed, the BMO should still contain the entire budget of highly incompatible elements of the whole mush layer, as no total refreezing during downward percolation should have occurred.

4.3. Implications for Earth evolution

Along these lines, we provide strong support for the formation of a thick BMO early in Earth's history. We prefer a batch-crystallization scenario of the deep MO, in which a BMO is formed due to compaction of a crystal mush with downward percolation of a liquid that is in equilibrium with 50% bridgmanite crystals (Fig. 5C). In this scenario, the initial composition of the BMO would be moderately FeO-enriched, as constrained by our melting experiments (Table 1). As found by the combination of our melting experiments and ab-initio calculations, the mush layer that undergoes downward compaction would have been very voluminous, reaching from ~1250 km depth down to the CMB. Also note that in this scenario, complete initial melting of the whole mantle with a MO that reaches the CMB is not required for the stabilization of a BMO. While giant-impact modeling suggests a deep extent of the MO in any case (Nakajima and Stevenson, 2015), a moderate depth extent of >1300 km should have been sufficient for BMO stabilization.

As the Earth evolves and cools over billions of years, the BMO continuously shrinks and becomes progressively iron-enriched. The compositional evolutions of the BMO and coexisting cumulates are not explicitly addressed by our study. However, iron and incompatible trace elements are expected to become enriched in the shrinking BMO due to their incompatible behavior, and to be primarily incorporated in the late-stage cumulates (or even any remaining liquids, see below). In any case, the freezing and related enrichment of the BMO is expected to occur on very long timescales (i.e., up to several Gyrs; Labrosse et al., 2007), mostly because heat transport due to solid-state convection in the overlying mantle is slow, but also because the progressive enrichment in iron systematically reduces the BMO melting curve.

Progressive iron enrichment in late-stage BMO cumulates can potentially stabilize a 'hidden geochemical reservoir' sufficiently dense to be isolated from global mantle convection. Such a reservoir has been suggested to be seismically evident as large low shear-wave velocity provinces in the lowermost mantle (Garnero and McNamara, 2008). BMO cumulates are expected to be enriched in bridgmanite in addition to iron (Ballmer et al., 2017), thereby reconciling the seismic characteristics of LLSVPs, e.g. in terms of the anti-correlation between shear-wave and bulk-sound speeds (Deschamps et al., 2012; Ballmer et al., 2016). Finally, the last droplets of the compositionally evolved BMO may be still stable at the CMB, and seismically visible as ultra-low velocity zones (ULVZ) (Garnero and McNamara, 2008).

5. Conclusions

We determine the density profile in the magma ocean during the first stages of its crystallization and up to the onset of the rheological transition from first-principles molecular dynamics calculations. We obtain the evolution of the chemical composition of both the melt and the bridgmanite crystals from DAC measurements at high pressures and temperatures. At 50% crystallization, close to the rheological transition, we find neutral buoyancy to occur around 50 GPa pressure. This leads to the formation of a mushy layer inside the MO, which further separates it into a shallow MO and a thick basal MO, both evolving independently later on.

The initial BMO is predicted to be moderately FeO-enriched when formed due to batch crystallization in MO. As the Earth cools over billions of years, the BMO continuously shrinks and becomes more iron-enriched. Progressive iron enrichment in a subset of the BMO cumulates can stabilize a 'hidden geochemical reservoir' sufficiently dense to be isolated from global mantle convection. BMO cumulates and residual melts are good candidates to host such reservoirs, and seismically evident in the lowermost mantle (Garnero and McNamara, 2008). In terms of incompatible elements that are partitioned into the shrinking BMO, the mass of the hidden reservoir is that of the mantle shell below the DCD. Thus, it corresponds to 7% of the mantle volume for fractional (Fig. 5A, B), and 40% for batch crystallization (Fig. 5C, D). For the more realistic batch crystallization scenario, such an enriched reservoir of ~40% in volume or ~50% in mass can host the missing 30–50% budget of highly incompatible elements (e.g., Boyet and Carlson, 2005), including radioactive isotopes and their daughters such as ^{40}Ar (Allègre et al., 1996) with implications for planetary thermal cooling.

Our results also suggest that terrestrial planets have evolved through a stage with two separate large-scale melt reservoirs if the depths of their MO were in excess of 50 GPa (~1300 km for

the Earth case). The shallow MO crystallized on a time scale of $\sim 10^6$–10^7 years (Solomatov, 2015; Bower et al., 2018), while the last liquid droplets of the BMO may still lurk close to the core–mantle boundary today (Labrosse et al., 2007). The initial composition of the BMO is constrained by our melting experiments. Further experimental and computational constraints are required to model the compositional evolution of the BMO, and comparison of any related predictions with the seismic structure of the deep mantle will improve our understanding of the Earth's long-term evolution.

Acknowledgements

This research was supported in part by the European Research Council (ERC) under the European Union's Horizon 2020 research and innovation program (grant agreement n° 681818 – IMPACT to RC) and by the JSPS (research grant 16H06285 to KH). RC acknowledges access to the GENCI supercomputers (Occigen, Ada, and Curie) through the stl2816 series of eDARI computing grants.

Appendix A. Supplementary material

Supplementary material related to this article can be found online at https://doi.org/10.1016/j.epsl.2019.03.031.

References

Abe, Y., 1995. Basic equations for evolution of partially molten mantle and core. In: Yukutake, T. (Ed.), The Earth's Central Part: Its Structure and Dynamics. TERRAPUB, Tokyo, pp. 215–230.
Allègre, C.J., Hofmann, A., O'Nions, K., 1996. The argon constraints on mantle structure. Geophys. Res. Lett. 23, 3555–3557.
Andrault, D., Bolfan-Casanova, N., Nigro, G.L., Bouhifd, M.A., Garbarino, G., Mezouar, M., 2011. Solidus and liquidus profiles of chondritic mantle: implication for melting of the Earth across its history. Earth Planet. Sci. Lett. 304, 251–259.
Andrault, D., Petitgirard, S., Lo Nigro, G., Devidal, J.L., Veronesi, G., Garbarino, G., Mezouar, M., 2012. Solid–liquid iron partitioning in Earth's deep mantle. Nature 487, 354–357.
Anisimov, V.I., Zaanen, J., Andersen, O.K., 1991. Band theory and Mott insulators: Hubbard U instead of Stoner I. Phys. Rev. B 44, 943–954.
Bajgain, S., Ghosh, D.B., Karki, B.B., 2015. Structure and density of basaltic melts at mantle conditions from first-principles simulations. Nat. Commun. 6, 8578.
Ballmer, M.D., Schumacher, L., Lekic, V., Thomas, C., Ito, G., 2016. Compositional layering within the large low shear-wave velocity provinces in the lower mantle. Geochem. Geophys. Geosyst. 17, 5006–5077.
Ballmer, M.D., Lourenço, D.L., Hirose, K., Caracas, R., Nomura, R., 2017. Reconciling magma-ocean crystallization models with the present-day structure of the Earth's mantle. Geochem. Geophys. Geosyst. 18, 2785–2806.
Bower, D.J., Sanan, P., Wolf, A.S., 2018. Numerical solution of a non-linear conservation law applicable to the interior dynamics of partially molten planets. Phys. Earth Planet. Inter. 274, 49–62.
Boyet, M., Carlson, R.W., 2005. ^{142}Nd evidence for early (<4.53 Ga) global differentiation of the silicate Earth. Science 309, 576–581.
Canup, R.M., 2012. Forming a Moon with an Earth-like composition via a giant impact. Science 338, 1052–1055.
Canup, R.M., Asphaug, E., 2001. Origin of the Moon in a giant impact near the end of the Earth's formation. Nature 412, 708–712.
Costa, A., Caricchi, L., Bagdassarov, N., 2009. A model for the rheology of particle-bearing suspensions and partially molten rocks. Geochem. Geophys. Geosyst. 10, Q03010.
Cuk, M., Stewart, S.T., 2012. Making the Moon from a fast-spinning Earth: a giant impact followed by resonant despinning. Science 338, 1047–1052.
Deschamps, F., Cobden, L., Tackley, P.J., 2012. The primitive nature of large low shear-wave velocity provinces. Earth Planet. Sci. Lett. 349–350, 198–208.
Dingwell, D.B., 2006. Transport properties of magmas: diffusion and rheology. Elements 2, 281–286.
Dufils, T., Folliet, N., Mantisi, B., Sator, N., Guillot, B., 2017. Properties of magmatic liquids by molecular dynamics simulation: the example of a MORB melt. Chem. Geol. 461, 34–46.
Elkins-Tanton, L.T., 2012. Magma oceans in the inner solar system. Annu. Rev. Earth Planet. Sci. 40, 113–139.
Fiquet, G., Auzende, A.L., Siebert, J., Corgne, A., Bureau, H., Ozawa, H., Garbarino, G., 2010. Melting of peridotite to 140 gigapascals. Science 329, 1516–1518.
Garnero, E.J., McNamara, A.K., 2008. Structure and dynamics of the Earth's lower mantle. Science 320, 626–628.
Ghosh, D.B., Karki, B.B., 2011. Diffusion and viscosity of Mg_2SiO_4 liquid at high pressure from first-principles simulations. Geochim. Cosmochim. Acta 75, 4591–4600.
Green, E.C.R., Artacho, E., Connolly, J.A.D., 2018. Bulk properties and near-critical behavior of SiO_2 fluid. Earth Planet. Sci. Lett. 491, 11–20.
Guilot, B., Sator, N., 2012. Noble gases in high-pressure silicate liquids: a computer simulation study. Geochim. Cosmochim. Acta 80, 51–69.
Hamano, K., Abe, Y., Genda, H., 2013. Emergence of two types of terrestrial planet on solidification of magma ocean. Nature 497, 607–610.
Hernandez, J.A., Caracas, R., 2016. Superionic-superionic phase transitions in body-centered cubic H_2O ice. Phys. Rev. Lett. 117, 135503.
Holland, T.J.B., Powell, R., 1998. An internally consistent thermodynamic data set for phases of petrological interest. J. Metamorph. Geol. 16, 309–343.
Ito, E., Kubo, A., Katsura, T., Walter, M.J., 2004. Melting experiments of mantle materials under lower mantle conditions with implications for magma ocean differentiation. Phys. Earth Planet. Inter. 143–144, 397–406.
Javoy, M., Kaminski, E., Guyot, F., Andrault, D., Sanloup, C., Moreira, M., Labrosse, S., Jambon, A., Agrinier, P., Davaille, A., Jaupart, C., 2010. The chemical composition of the Earth: enstatite chondrite models. Earth Planet. Sci. Lett. 293, 259–268.
Karki, B.B., 2010. First-principles molecular dynamics simulations of silicate melts: structural and dynamical properties. Rev. Mineral. Geochem. 71, 355–389.
Kresse, G., Hafner, J., 1993. Ab initio molecular dynamics for liquid metals. Phys. Rev. B 47, 558.
Labrosse, S., Hernlund, J.W., Coltice, N., 2007. A crystallizing dense magma ocean at the base of the Earth's mantle. Nature 450, 866–869.
Lebrun, T., Massol, H., Chassefière, E., Davaille, A., Marcq, E., Sarda, P., Leblanc, F., Brandeis, G., 2013. Thermal evolution of an early magma ocean in interaction with the atmosphere. J. Geophys. Res., Planets 118, 1155–1176.
Lock, S.J., Stewart, S.T., Petaev, M.I., Leinhardt, Z., Mace, M.T., Jacobsen, S.B., Cuk, M., 2018. The origin of the Moon within a terrestrial synestia. J. Geophys. Res., Planets 123, 910–951.
McDonough, W.F., Sun, S.S., 1995. The composition of the Earth. Chem. Geol. 120, 223–253.
Nakajima, M., Stevenson, D.J., 2015. Melting and mixing states of the Earth's mantle after the Moon-forming impact. Earth Planet. Sci. Lett. 427, 286–295.
Nomura, R., Ozawa, H., Tateno, S., Hirose, K., Hernlund, J., Muto, S., Ishii, H., Hiraoka, N., 2011. Spin crossover and iron-rich silicate melt in the Earth's deep mantle. Nature 473, 199–203.
Nomura, R., Hirose, K., Uesugi, K., Ohishi, Y., Tsuchiyama, A., Miyake, A., Ueno, Y., 2014. Science 343, 522–525.
Palme, H., O'Neill, H.S.C., 2003. Cosmochemical estimates of mantle composition. In: Holland, H.D., Turekian, K.K. (Eds.), Treatise on Geochemistry, vol. 2. Elsevier-Pergamon, Oxford, pp. 1–39.
Perdew, J.P., Burke, K., Ernzerhof, M., 1996. Generalized gradient approximation made simple. Phys. Rev. Lett. 77, 3865.
Pradhan, G.K., Fiquet, G., Siebert, J., Auzende, A., Morard, G., Antonangeli, D., Garbarino, G., 2015. Melting of MORB at core–mantle boundary. Earth Planet. Sci. Lett. 431, 247–255.
Solomatov, V.S., 2015. Magma oceans and primordial mantle differentiation. In: Schubert, G. (Ed.), Treatise on Geophysics, vol. 9. Elsevier-Pergamon, Oxford, pp. 81–104.
Solomatov, V.S., Olson, P., Stevenson, D.J., 1993. Entrainment from a bed of particles by thermal-convection. Earth Planet. Sci. Lett. 120, 387–393.
Stixrude, L., Karki, B.B., 2005. Structure and freezing of $MgSiO_3$ liquid in Earth's lower mantle. Science 310, 297–299.
Stixrude, L., de Koker, N., Sun, N., Mookherjee, M., Karki, B.B., 2009. Thermodynamics of silicate liquids in the deep Earth. Earth Planet. Sci. Lett. 278, 226–232.
Suzuki, A., Ohtani, E., 2003. Density of peridotite melts at high pressure. Phys. Chem. Miner. 30, 449–456.
Takahashi, E., 1986. Melting of a dry peridotite KLB-1 up to 14 GPa: implications on the origin of peridotitic upper mantle. J. Geophys. Res. 91, 9367–9382.
Tateno, S., Hirose, K., Ohishi, Y., 2014. Melting experiments on peridotite to lowermost mantle conditions. J. Geophys. Res., Solid Earth 119, 4684–4694.
Tonks, W.B., Melosh, H.J., 1990. The physics of crystal settling and suspension in a turbulent magma ocean. In: Newsom, N.E., Jones, J.H. (Eds.), Origin of the Earth. Oxford Univ. Press, New York, pp. 151–174.
Vuilleumier, R., Sator, N., Guillot, B., 2009. Computer modeling of natural silicate melts: what can we learn from ab initio simulations. Geochim. Cosmochim. Acta 73, 6313–6339.
Wade, J., Wood, B.J., 2012. Metal–silicate partitioning experiments in the diamond anvil cell: a comment on potential analytical errors. Phys. Earth Planet. Inter. 192–193, 54–58.